

Observation of Multiple Vibrational Modes in Ultrahigh Vacuum Tip-Enhanced Raman Spectroscopy Combined with Molecular-Resolution Scanning Tunneling Microscopy

N. Jiang,[†] E. T. Foley,^{†,‡} J. M. Klingsporn,[†] M. D. Sonntag,[†] N. A. Valley,[†] J. A. Dieringer,[†] T. Seideman,[†] G. C. Schatz,[†] M. C. Hersam,^{*,†,‡} and R. P. Van Duyne^{*,†}

[†]Department of Chemistry, and [‡]Department of Materials Science and Engineering, Northwestern University, Evanston, Illinois 60208, United States

S Supporting Information

ABSTRACT: Multiple vibrational modes have been observed for copper phthalocyanine (CuPc) adlayers on Ag(111) using ultrahigh vacuum (UHV) tip-enhanced Raman spectroscopy (TERS). Several important new experimental features are introduced in this work that significantly advance the state-of-the-art in UHV-TERS. These include (1) concurrent sub-nm molecular resolution STM imaging using Ag tips with laser illumination of the tip-sample junction, (2) laser focusing and Raman collection optics that are external to the UHV-STM that has two cryoshrouds for future low temperature experiments, and (3) all sample preparation steps are carried out in UHV to minimize contamination and maximize spatial resolution. Using this apparatus we have been able to demonstrate a TERS enhancement factor of 7.1×10^5 . Further, density-functional theory calculations have been carried out that allow quantitative identification of eight different vibrational modes in the TER spectra. The combination of molecular-resolution UHV-STM imaging with the detailed chemical information content of UHV-TERS allows the interactions between large polyatomic molecular adsorbates and specific binding sites on solid surfaces to be probed with unprecedented spatial and spectroscopic resolution.

KEYWORDS: *tip-enhanced Raman spectroscopy, scanning tunneling microscopy, ultrahigh vacuum, phthalocyanine, density functional theory*

Tip-enhanced Raman spectroscopy (TERS) has emerged over the past decade as an effective technique for studying surface science with unprecedented molecular detail.^{1–3} TERS combines the surface imaging capabilities of scanning probe microscopy (SPM) with the rich chemical information content of vibrational Raman spectroscopy. These two techniques complement each other and provide quantitative information on surface morphology, binding sites, and the vibrational fingerprint of adsorbates on solid substrates. Optical excitation of a noble metal SPM probe excites its localized surface plasmon resonance (LSPR), creating a highly confined electromagnetic field at the tip-sample junction. Field localization at the tip allows TERS to overcome the diffraction limited resolution of conventional Raman spectroscopy and provides a Raman enhancement on the order of 10^6 – 10^7 .^{4–6} Even though TERS has been successfully used to study carbon nanotubes,^{7–9} graphene,¹⁰ quantum dots,¹¹ and biological systems,^{12–14} in ambient environments, its full potential has not yet been realized.

Essential to the TERS experiment, SPM has been developed over the last three decades to study single molecules and molecular assemblies.¹⁵ As an important member of the SPM family, the scanning tunneling microscope (STM), which is based on the electronic interactions between an adsorbate/surface system and a metal probe, provides topographic and electronic structure information down to the atomic scale. In addition, the development of STM-based inelastic electron tunneling spectroscopy (IETS) has successfully demonstrated

vibrational spectroscopy for few-atom molecules, making possible the identification of individual vibrational modes for adsorbates on conductive surfaces.^{16–18} However, the need for cryogenic temperatures, relaxed selection rules, and relatively low chemical information content has limited IETS to a small class of low-molecular weight species.¹⁹

Combining STM and TERS provides an alternative method to study vibrational, rotational, and other low-frequency modes of molecules, which not only chemically identifies the molecules adsorbed on a surface; but, also yields information about adsorption configuration and chemical bonding in or between molecules. Steidtner and Pettinger acquired the first concurrent STM topographic images and TER spectra using a gold STM probe in ultrahigh vacuum (UHV).^{20,21} Although these authors reported single molecule sensitivity, the TER spectra included only one or two peaks, which is not sufficient to establish the identity and structural integrity of large polyatomic molecular adsorbates. Similarly, the observation of multiple vibrational modes is required to fully characterize the interaction and orientation of large polyatomic molecular adsorbed on a solid surface. Furthermore, their sample preparation occurred ex situ, which likely implied surface contamination that may have compromised the spatial resolution and quality of the STM topography and TER

Received: November 12, 2011

Revised: December 22, 2011



spectra. Preparing samples in UHV is essential for maintaining atomically clean surfaces, which greatly enhances the stability of the tip–sample junction in UHV STM, and ensures minimal contamination in the field enhancement region beneath the STM tip in TERS measurements.

Herein, we present UHV-TERS spectra for ordered copper phthalocyanine (CuPc) adlayers on Ag(111) that display multiple vibrational modes as well as concurrent UHV-STM images with sub-nm molecular resolution STM topography. Phthalocyanines have attracted significant interest for potential application in organic light-emitting diodes (OLED), thin-film transistors (TFTs), dye-sensitized solar cells, as well as other optical and electronic applications.^{22–24} CuPc, as one member of the phthalocyanine family, is a large polyatomic molecule with D_{4h} symmetry that assembles into highly ordered adlayers on a variety of substrates.^{25–29} The ordered structure of CuPc for the monolayer on Ag(111) makes the observation of molecular topography possible at room temperature, however, the unambiguous chemical identification requires observation of several TERS vibrational modes. For these reasons, CuPc is an ideal model system for demonstrating concurrent UHV-TERS and UHV-STM imaging.

Since a pristine UHV environment is required for the highest quality data, all sample preparation and tip degassing are performed in situ. Furthermore, the laser focusing and Raman collection optics are constructed external to the UHV chamber, thus allowing for modification of the optical path without compromising the UHV base pressure of less than 5×10^{-11} Torr. With laser illumination of the tip–sample junction, sub-nm molecular resolution STM images and multivibration TERS spectra are acquired using a Ag tip at room temperature. The STM images reveal subtle features in the CuPc adlayer including the orientation and boundaries between ordered molecular domains. The TERS electromagnetic enhancement factor is shown to be 7.1×10^5 , and density functional theory (DFT) calculations show that eight distinct vibrational modes for CuPc can be quantitatively assigned. The ability to resolve multiple vibrational peaks while concurrently achieving sub-nm molecular resolution topographic imaging allows the relationship between many-atom adsorbates and solid surfaces to be quantitatively and unambiguously interrogated, thus presenting new opportunities for the study of catalysis, surface functionalization, and related interfacial phenomena.

The experiments were performed with a cryogenic variable temperature UHV-STM with a base pressure in the range of 10^{-11} Torr.³⁰ The single crystal Ag(111) substrate (one side polished $<0.03 \mu\text{m}$, orientation accuracy $<0.1^\circ$) was purchased from Princeton Scientific Corp. The clean Ag(111) surface was prepared by repeated cycles of Ar ion sputtering and annealing at 480°C . CuPc (Aldrich, $>99.99\%$) molecules were thermally sublimed at 280°C onto the Ag(111) surface that was maintained at room temperature. The CuPc evaporation rate was approximately 0.033 ML/min. All STM measurements were conducted at room temperature. The voltages are applied to the sample with respect to the grounded tip, and the images are gathered in constant-current mode.

Ex-situ optics were used for laser focusing on the tip–sample junction and the collection of Raman scattered light (Figure 1). Eliminating internal optics allowed for modification of the optical path without affecting the UHV base pressure of less than 5×10^{-11} Torr. A 632.8 nm HeNe laser (Research Electro-optics, 17.0 mW) was expanded to a beam diameter of approximately 25 mm and focused on the tip–sample junction

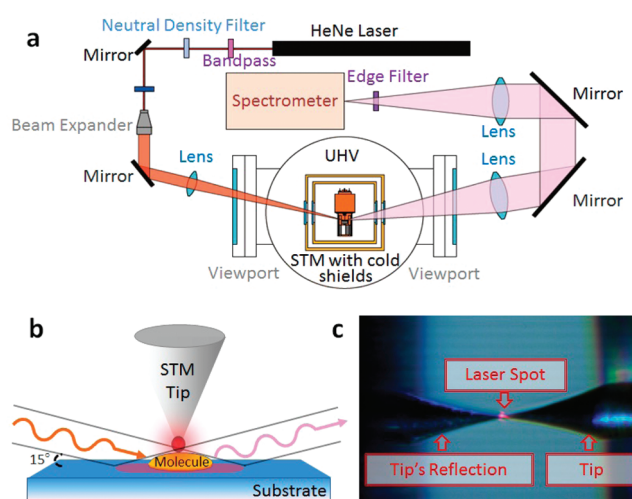


Figure 1. (a) Schematic of the experimental apparatus. (b) Schematic depiction of the tip–sample junction. The STM tip is not only used for topographic imaging; but, also as a plasmonic enhancer of Raman scattered light. (c) CMOS camera image of the tip(Ag)–sample(Ag(111)) junction.

with polarization along the tip-axis. An external CMOS camera was used to visualize the focusing operation in real time. Laser access to the sample in UHV was provided through a 7056 glass viewport on the UHV chamber and two sapphire windows in the STM cryostat. The angle of incidence was 75° with respect to the sample normal. The laser spot on the sample surface at optimum focus was found to be elliptical in the sharp with major axis = $60 \mu\text{m}$ and minor axis = $40 \mu\text{m}$ (vide infra).

Raman scattered light was collected at angle of 75° from the surface normal through two sapphire windows and a 7056 glass window on the opposing side. Residual laser light was filtered from the Raman signal, which was then focused onto a $100 \mu\text{m}$ slit of a 1/2 m imaging spectrograph (Acton Spectropro 500i), equipped with a liquid nitrogen cooled CCD (Acton Spec-10, 1340×400 pixel). All spectra were recorded with a 1200 L/mm grating blazed at 500 nm and centered at a Raman shift of 1250 cm^{-1} .

Electrochemically etched Ag STM probes were prepared using a technique adapted from Zhang et al.⁶ A platinum ring with a diameter of 20 mm was used as a counter-electrode and positioned at the surface of a 3.3 M perchloric acid ethanolic solution. A linear micrometer was used to immerse a short length of Ag wire (99.9%, 0.25 mm, Alfa Aesar) into solution. A potential of 1.6 V was applied between the silver wire and the platinum ring with a potentiostat (CH Instruments). A custom Ag/AgCl ethanolic reference electrode provided a reference potential to complete the three-electrode geometry. Etching of the silver wire is confined near the meniscus formed between the silver wire and etching solution. Potentiostatic control of Ag tip etching provides a more precise control of etching potential and allows current-cutoff capabilities. A stereoscopic microscope was used to monitor the etching process and to properly adjust the Ag wire depth. After etching, tips were rinsed in warm deionized water (Millipore) followed by ethanol. Prior to introduction to the UHV chamber, the Ag tips were degassed in the loadlock at more than 100°C in high vacuum ($\sim 10^{-9}$ Torr) for more than 12 h. This technique produces highly reproducible plasmonic probes with a radius of curvature of approximately 100 nm (Figure 3a). Probe morphology was studied by SEM analysis (Hitachi S-4800-II).

A CuPc SERS reference was acquired from a silver film over nanosphere (AgFON) substrate.³¹ The AgFON substrate was prepared on a silicon substrate using 590 nm silicon spheres, optimized for 633 nm excitation, and covered with 200 nm of silver (custom thermal evaporation system). CuPc molecules were sublimed onto the AgFON substrate in UHV using the same molecular coverage as was used on the Ag(111) surface. The substrates were also analyzed under ambient conditions utilizing a fiber-coupled solid-state diode laser providing 640 nm excitation. Scattered light was collected through the excitation lens and focused onto a fiber optic cable coupled to the same spectrograph utilized for UHV-TERS.

The electronic structure calculations and simulated Raman spectra presented in this work were performed using the Amsterdam Density Functional (ADF) program package.³² Full geometry optimization and frequency calculations for isolated phthalocyanines were completed using the Becke-Perdew (BP86) XC-potential and a triple- ζ polarized Slater type (TZP) basis set. Polarizabilities for the closed shell molecules were calculated at the same level of theory using the AOResponse module. Polarizabilities on resonance were calculated using a global damping parameter of $\Gamma = 0.004$ au (0.1 eV); this is the same as was used in earlier work³³ and is thought to represent a reasonable estimate of the excited state dephasing lifetime. Excitation energies and oscillator strengths are calculated using the Excitations module for the lowest 200 dipole allowed transitions.

Raman intensities are presented as scattering cross sections calculated by³⁴

$$\frac{d\sigma}{d\Omega} = \frac{\pi^2}{\epsilon_0^2} (\omega - \omega_p)^4 \frac{\hbar}{8\pi^2 c \omega_p} [45\bar{\alpha}'_p{}^2 + 7\gamma'_p{}^2] \frac{1}{45(1 - e^{(-\hbar c \omega_p / k_B T)})}$$

where ω and ω_p are the frequencies of the incident radiation and the p th vibrational mode, respectively, and the scattering factor $45\bar{\alpha}'_p{}^2 + 7\gamma'_p{}^2$ is composed of the isotropic ($\bar{\alpha}'_p$) and anisotropic (γ'_p) polarizability derivatives with respect to the p th vibrational mode.

All metal phthalocyanines have a similar molecular structure, containing a central metal atom surrounded by a phthalocyanine framework. CuPc is a typical planar metal phthalocyanine molecule as schematically shown in Figure 2a. CuPc molecules were thermally sublimed onto the Ag(111) surface that was maintained at room temperature. At low coverage, no CuPc molecules can be observed on the terrace by STM. With increasing molecular coverage, a highly ordered CuPc monolayer is formed, as shown in Figure 2b.²⁵ Like the FePc molecules on Au(111) surfaces, the coverage is determined by the competition between molecule–substrate and molecule–molecule interactions.^{35,36} At lower coverage, CuPc molecules are free to diffuse on the Ag(111) surface, and are not visible in STM images at room temperature. It is only at saturation coverage, where the motion of CuPc molecules is constrained by neighboring CuPc molecules, that an ordered adlayer is observed. The molecule–substrate interactions then play a role in the formation of molecular domains that are commensurate with the underlying Ag(111) substrate.

Due to the 3-fold symmetry of the Ag(111) substrate, three symmetry-equivalent domains of the monolayer are observed in our STM results. Figure 2b also shows domain boundaries

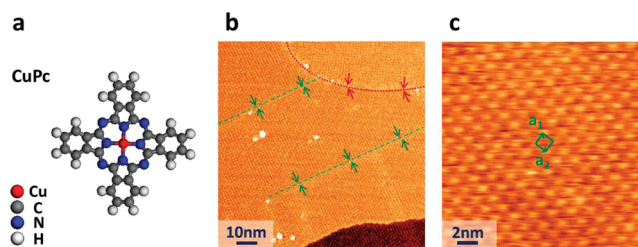


Figure 2. (a) Chemical structure of CuPc. (b) Large scale STM image (100 nm \times 100 nm) of a well-ordered CuPc adlayer on a Ag(111) surface measured with a Ag tip. Different orientations of molecular domains are colored by red and green arrows. The domain boundary between the same symmetry domains is marked by green dashed lines, and the domain boundary between the different symmetry domains is marked by red dotted lines. (c) High resolution STM image (20 nm \times 20 nm) of the CuPc closed packed structure. The unit cell is indicated with the green square. (STM imaging conditions: $V = +0.5$ V, $I = 0.1$ nA).

between symmetry-equivalent domains. The domain boundaries, marked by green dashed lines in Figure 2b, are line defects that mark a periodically shifted lattice within two parts of a domain. The domain boundaries between two distinct molecular orientations are marked by the red dotted lines. Note that a single orientation domain can be observed on different terraces of the Ag(111) substrate, which indicates that the molecular layer can extend over several different steps of various heights. At higher resolution (Figure 2c), the CuPc molecules formed on the terraces of the Ag(111) show that the planar skeleton is parallel to the metal surface. A square unit cell is marked by green lines, in which the green arrows (a_1 , a_2) represent the unit cell vectors of the molecular superstructure.

Irradiating the tip–sample junction with excessively high CW laser power can make STM scanning unstable, mainly due to thermal expansion of the Ag tip. A stable and clear STM image is necessary in order to correlate the spatial information of molecular adsorbates with the chemical information provided by TERS. To optimize the quality of the STM imaging under laser irradiation, a Si(100) surface with thermally sublimed CuPc molecules was scanned at room temperature. The scan shows atomic resolution dimer rows with submolecular resolution CuPc molecules, after the Ag tip had been irradiated with 7.0×10^4 W/cm² CW laser for 1 h to stabilize thermal drift (20 nm \times 20 nm STM image is shown in the Supporting Information). The power density of the CW laser is estimated by taking into account a 38% power loss through the sapphire windows and UHV viewport glass. This value was determined from measured reflection losses through these materials. An identical loss in the scattering intensity is also experienced, thus reducing the overall collection efficiency. Obtaining stable and clear STM images with a laser-illuminated plasmonic Ag tip is a prerequisite to achieving correlated atomic-scale spatial information with TER spectra.

Figure 3b shows a molecular resolution STM image of CuPc on Ag(111) obtained with a 130 nm radius of curvature Ag tip (Figure 3a) irradiated with a 9.4×10^5 W/cm² CW laser. UHV-TERS spectra of CuPc on Ag(111) were acquired and clearly show all the vibrational features observed in the CuPc SERS reference sample (Figure 3c). TER spectra were taken while the tip was maintained in tunneling range by the STM feedback loop. Peaks not attributable to CuPc at 1374 and 1403 cm⁻¹ are assigned to sapphire modes from the STM cryostat windows that provide optical access to the tip–sample junction. When

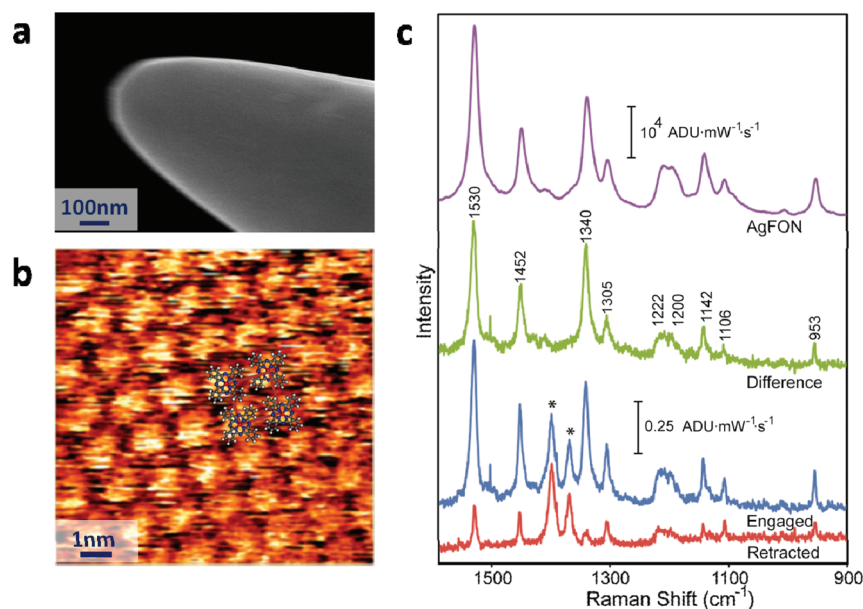


Figure 3. (a) SEM image of a silver tip showing a radius of curvature at the apex of 130 nm. (b) Molecular resolution topographic STM image ($10 \text{ nm} \times 10 \text{ nm}$) of a CuPc adlayer on Ag(111) with the tip illuminated by the CW laser. (STM imaging condition: $V = +1.5 \text{ V}$, $I = 0.3 \text{ nA}$). (c) UHV-TERS spectra of a CuPc adlayer on Ag(111) and SERS spectrum of a CuPc adlayer on AgFON. The asterisks (*) indicate peaks at 1374 and 1403 cm^{-1} that result from the sapphire windows.

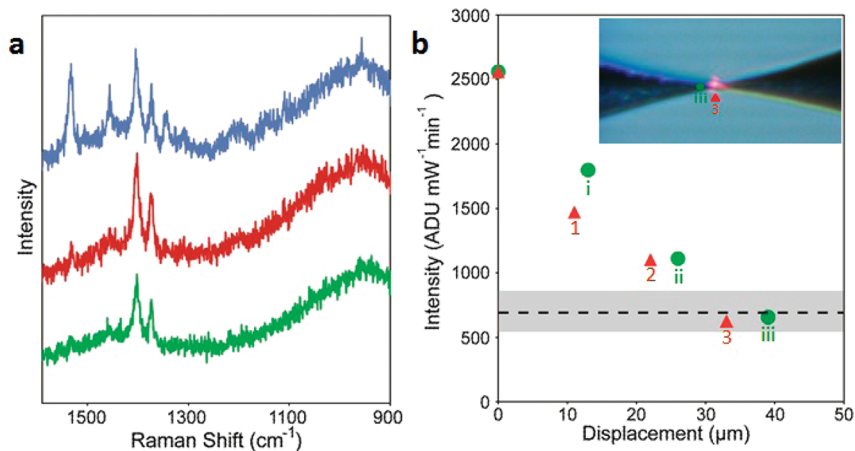


Figure 4. (a) UHV-TER spectra measured with the laser spot focused at different locations. The blue spectrum was collected with the laser spot centered on the tip–sample junction, while the red and green spectra were collected with the laser spot on the sample only and probe shank only, respectively. (b) Laser spot position dependence of the intensity of the 1530 cm^{-1} peak in the Raman spectra. The dashed line shows the average retracted signal with the range of values observed indicated by the gray bar. The inset shows the displacement of the laser spot on the CMOS image.

the plasmonic STM probe is near the surface, an enhancement of the signal is observed from the intense localized electromagnetic field created at the tip–sample junction.

Retraction of the probe out of the tunneling condition shows a clear decrease in intensity of the CuPc spectral features. The residual intensity when retracted matches the intensity observed when the laser is focused off of the tip–sample junction. This observation implies that the residual signal is resonant Raman scattering from the CuPc monolayer on the Ag(111) surface (Figure 3c). A resonance enhancement of the CuPc Raman scattering occurs because the excitation energy matches that of the $\sim 650 \text{ nm}$ electronic transition of CuPc. Additionally, a laser power density of $9.4 \times 10^5 \text{ W/cm}^2$, large excitation and collection volumes, and long acquisition times increased the retracted CuPc signal, which is useful since this residual intensity facilitates system alignment. The intensity

difference between the engaged and retracted spectra indicates the TERS component of the acquired Raman spectra.

In order to measure the TERS enhancement factor, a method to determine the laser focal area without compromising UHV conditions is required. The focal volume was determined by observing the signal intensity as the excitation source was spatially translated both vertically and horizontally across the tip–sample junction. Analysis of the integrated Raman intensity involved performing a baseline subtraction and fitting the 1530 cm^{-1} mode to a Lorentzian function. The integrated intensity as a function of position shows a decrease in signal intensity as the laser is moved away from the tip–sample junction (Figure 1c). The TERS intensity is found to approach the background signal with a movement of less than $40 \mu\text{m}$. The average integrated background signal observed from thirteen acquisitions is indicated by a dashed line with a surrounding gray region

indicating the range of intensity values observed with the STM probe retracted (Figure 4). Note that this data set was taken with a different probe exhibiting a different background TERS signal than that depicted in Figure 3c. In tips that yield high intensity TERS spectra for CuPc on Ag(111), there is significant tip-to-tip variation in the overall intensity of peaks in the Raman spectra; however, the location of these peaks and their relative intensities are highly reproducible. Spectra with no displacement of the laser focal volume and with maximum displacement, in both the vertical and horizontal directions, are also displayed. These measurements allow the spot size to be determined in both the horizontal and vertical directions. A Gaussian function was fit to the intensity as a function of laser displacement. To fit a full Gaussian profile to this data set, the data were mirrored around the point of zero displacement. Using this method, the 10:90 beam profile was found to be 60 μm in the horizontal dimension and 40 μm in vertical dimension. An elliptical beam profile is expected because of the glancing angle of excitation of the tip-sample junction.

Using the measured far-field focal spot size, surface coverage, engaged and retracted intensities, and the estimated tip enhancement area, the TERS enhancement factor (EF) is calculated using the following equation:

$$EF_{\text{TERS}} = \frac{(I_{\text{engaged}} - I_{\text{retracted}})/N_{\text{TERS}}}{I_{\text{retracted}}/N_{\text{background}}} \\ = \left(\frac{I_{\text{engaged}}}{I_{\text{retracted}}} - 1 \right) \frac{N_{\text{background}}}{N_{\text{TERS}}}$$

Analysis of the intensity is straightforward; however, care must be taken in the calculation of the number of molecules probed in each case. Due to the larger laser spot size, the retracted signal originates from the number of molecules contained within the laser focal area. The number of CuPc molecules probed in the retracted case was determined to be 3.2×10^9 using a packing density of 0.59 molecules/ nm^2 as determined by STM. In the TERS case, the number of molecules probed is dependent on the TERS enhancement area. The STM tip has a 130 nm radius of curvature leading to an enhancing region with a radius of 65 nm containing 2.3×10^4 CuPc molecules, based on a Gaussian profile of the enhancing field.³⁷ The enhancement factor for the TERS spectrum of CuPc was therefore calculated as 7.1×10^5 based on the enhancement of the 1530 cm^{-1} peak. It should be noted that the TERS enhancement factor is dependent on the value of the TERS enhancement area. We have used Pettinger's method which calculated the enhancing region as either the full, or half the radius of curvature of the plasmonic probe.³⁷ However, with the large radius of curvature of the probe used for these results, the enhancing region is almost certainly overestimated. The enhancing region is more likely much smaller and can be viewed as an enhancing hot-spot with much higher electromagnetic field experienced at the directly under the tip apex.^{38,39} Consequently, our estimated TERS enhancement factor of 7.1×10^5 should be viewed as the lowest possible value consistent with the data. Additionally, the engaged TERS spectrum shows a signal-to-noise ratio of approximately 20 for the 1530 cm^{-1} peak. A high signal-to-noise ratio with an enhancement factor of 7.1×10^5 illustrates the possibility of performing site-specific studies in UHV using ex-situ optics on samples prepared completely under UHV conditions.

To understand the first UHV-TER spectra displaying multiple vibrational modes and concurrent molecular-scale topographic STM imaging, electronic structure calculations and simulated Raman spectra were carried out using the ADF program package. Optimized geometries for both CuPc and ZnPc in the gas phase were calculated using the ADF software. Both molecules adopt a planar geometry with D_{4h} point group symmetry. Bond lengths and angles were found to be in agreement with previous DFT calculations by Basova et al.⁴⁰ (for CuPc) and Murray et al.⁴¹ (for ZnPc) as well as with crystallographic data.⁴²

The calculated vibrational frequencies agree with the aforementioned theoretical and experimental measurements. Table 1 compares a set of vibrational frequencies calculated

Table 1. Selected Vibrational Modes Determined Experimentally for CuPc and with DFT Calculations for CuPc and ZnPc^a

exp CuPc (cm^{-1})	DFT ZnPc (cm^{-1})	DFT CuPc (cm^{-1})	
	670	674	in plane full symmetric nonmetal bound N-M stretch and outer ring stretches
	742	737	in plane ring symmetric N-M stretch
	831	830	in plane full symmetric N-M stretch
953	931	938	in plane diag symmetric N-M-N bend and N-M stretch
1106	1098	1098	in plane diag symmetric N-M-N bend
1142	1132	1133	in plane ring symmetric and outer rings breathing
1200	1196	1193	in plane diag symmetric N-M-N bend
1305	1287	1290	in plane diag symmetric outer ring rotations
1340	1343	1343	in plane full symmetric N-C stretch and ring C-C stretch
	1367	1369	in plane ring symmetric outer ring C-C stretch
1452	1434	1438	in plane ring symmetric outer ring C-C stretch
	1419	1439	in plane diag symmetric nonmetal bound N-C stretch
1530	1526	1545	in plane ring symmetric non metal bound N-C stretch

^aM: the metal center of metal phthalocyanine molecules. Each mode has its motions detailed.

with DFT and determined using TERS. The atomic motions involved in each selected mode are also detailed. For the majority of the modes, substituting Cu with Zn results in minor changes (energy changes $<10 \text{ cm}^{-1}$). Vibrations that involve C-N stretches with the N atom not bound to the central metal atom are much more sensitive to the change with a shift of around 20 cm^{-1} . Experimental spectra are measured with the molecules interacting with a silver surface, whereas the DFT calculations are for the free molecule, thus explaining the difference in the experimental and DFT results.

Time dependent DFT calculations show two strong electronic transitions around 631.5 nm for ZnPc. The majority (90.5%) of these transitions correspond to an excitation from the HOMO to one of the two degenerate LUMOs. HOMO and LUMO orbitals are shown in Figure 5a. While the excitations calculation has not been performed on the open shell CuPc due to software limitations, the effect of changing the central metal atom is expected to be very localized. Multipole derived charge (MDC) spin densities are large for

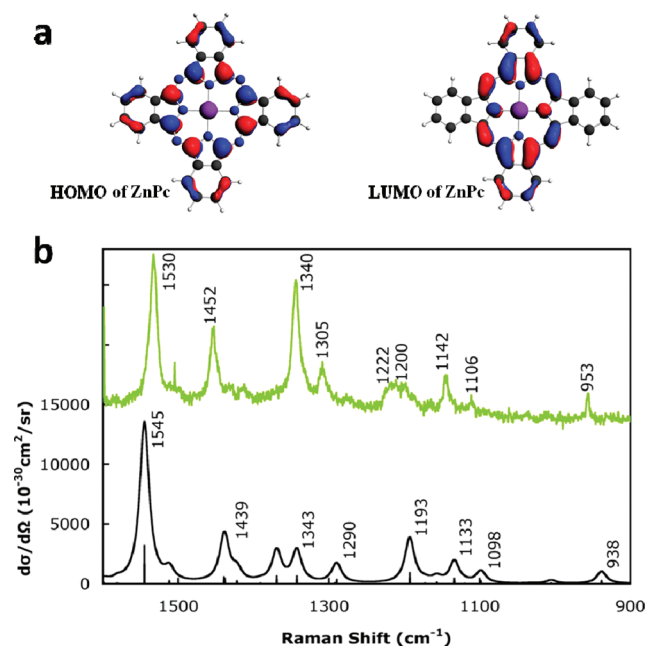


Figure 5. (a) HOMO and LUMO orbitals of ZnPc. (b) Simulated resonance Raman spectrum (black) of CuPc constructed using ZnPc resonance Raman intensities at an incident wavelength of 631.48 nm. The differential cross section is given in units of $10^{-30} \text{cm}^2/\text{sr}$. Peaks are broadened by a Lorentzian with a full width at half-maximum of 15 cm^{-1} . The scale is for the broadened spectrum. Experimental TER spectrum (green) is displayed for comparison.

Cu (0.409), moderate for the N bound to Cu (<0.233), smaller for the C bound to the N (<0.068), and negligible for the rest of the molecule ($<\sim 0.01$). Atomic orbitals of the metal atom are not involved in the molecular orbitals that correspond to the ZnPc HOMO and LUMOs. Therefore, these orbitals remain qualitatively unchanged. The orbital energy gap changes from 1.425 eV for ZnPc to between 1.430 and 1.442 eV for CuPc. It is therefore expected that CuPc should have transitions near 630 nm that are very similar to those seen for ZnPc. With the experimental incident wavelength of 633 nm, it is assumed that the experiments are being performed on molecular resonance. Optimized geometry coordinates and a complete list of vibrational frequencies can be found in the Supporting Information.

Currently, it is not possible to perform direct calculations of resonance Raman intensities of open-shell molecules with ADF. Two properties of CuPc allow an indirect calculation of the resonance Raman spectrum. First, vibrational modes with non-negligible Raman intensities change minimally with substitution of the central metal and do not involve motion of the metal atom. Second, the molecular orbitals involved in the excitation of interest do not have a strong dependence on the metal atom. Given the unique nature of the metal phthalocyanines, it is reasonable to use the resonance Raman intensities from calculations on ZnPc to generate a spectrum for CuPc.

Resonance Raman intensities for ZnPc were calculated using polarizability derivatives determined using finite differencing. All vibrational modes between 300 and 2000 cm^{-1} for CuPc were analyzed and matched to the corresponding vibration of ZnPc. Resonance Raman intensities were assigned to the matched CuPc mode and the resulting stick spectrum was convoluted using Lorentzians with a width of 15 cm^{-1} . The

resulting spectrum is presented in Figure 5b alongside the experimental spectrum.

Differences between the calculated and experimental spectra are minor when considering that the experimental peaks may be shifted by interaction with the silver surface. The calculated spectrum has only one peak, at 1193 cm^{-1} , whereas the experimental spectrum has a very broad peak centered around 1210 cm^{-1} . This may be due to surface effects as the CuPc likely adopts multiple bonding geometries. The different bonding geometries could have a strong influence on the N–Cu–N in-plane bending, which is the major motion in only the 1193 and 1098 cm^{-1} peaks. The weakness of the 1098 cm^{-1} peak may make the disorder more difficult to see. Calculations also predict a peak at 1369 cm^{-1} , which is not generally observed in the experiments. This vibrational mode has a large portion of its motion in the C–C bond stretch on the extreme edge of the outer rings. The polarizability derivative normal to the molecular plane for this mode is small compared to the observed peaks, which suppresses the peak 1369 cm^{-1} when the molecule is flat on the surface. Overall, the strong agreement between theory and experiment allows unambiguous identification of the CuPc vibrational modes in the TER spectra.

The orientationally averaged, gas phase, calculated spectrum is dominated by in-plane vibrational modes. Nevertheless, it reproduces the number of peaks and the intensity of the experimental spectrum for CuPc lying flat on the surface. The strong enhancement of the field normal to the surface combined with the planar structure of CuPc might be expected to give rise to strongly enhanced out-of-plane modes. Out-of-plane modes do not contribute strongly for two reasons. First, there are no out-of-plane modes above 1000 cm^{-1} . In addition, analysis of the Raman tensor shows that the spectrum will remain relatively unchanged unless the plane of the molecule and the plane of the surface are strictly parallel. This is particularly true for the modes in the 900 to 1700 cm^{-1} range that were observed in the experimental TER spectra. Accounting for thermal fluctuations and a nonideal surface, it is expected that the in-plane vibrational modes will be dominant. It is predicted, that under different conditions, peaks due to the orientation of the molecule could be observed. The Raman tensors for some selected vibrational modes can be found in the Supporting Information.

The combination of UHV-STM and TERS provides a unique opportunity to study adsorbates with unprecedented spectral and spatial resolution. UHV-STM with a laser illuminated plasmonic tip yields atomic resolution electronic structure and topography, while correlated UHV-TERS provides detailed multivibrational spectroscopic information that enables chemical identification of large polyatomic adsorbates. In particular, we have shown subnm molecular resolution images of CuPc in an ordered adlayer on Ag (111) that are correlated with TER spectra that possess eight distinct vibrational modes of CuPc using a plasmonic Ag tip with an enhancement factor of 7.1×10^5 . This work sets the stage for Raman vibrational fingerprinting and correlated submolecular resolution topography of site-specific binding of high molecular weight species on solid surfaces. Such studies are likely to provide new insight into many widely studied systems, including organic semiconductors, dye-sensitized solar cells, photovoltaics, and catalysts.

■ ASSOCIATED CONTENT

● Supporting Information

STM of CuPc on Si(100), calculated geometries, frequencies, and Raman tensors for selected modes of CuPc and ZnPc. This material is available free of charge via the Internet at <http://pubs.acs.org>.

■ AUTHOR INFORMATION

Corresponding Author

*E-mail: vanduyne@northwestern.edu. Phone: 847-491-3516. Fax: 847-491-7713 (R.P.V.D.). E-mail: m-hersam@northwestern.edu. Phone: 847-491-2696. Fax: 847.491.7820 (M.C.H.).

■ ACKNOWLEDGMENTS

This work was supported by the National Science Foundation (CHE-0802913, CHE-0911145, CHE-0955689, EEC-0647560, EEC-0634750, and DMR-1121262), AFOSR/DARPA Project BAA07-61 (FA9550-08-1-0221), and the Department of Energy Basic Energy Sciences (DE-FG02-09ER161 09, DE-FG02-03ER15457, and DE-SC0001785). Further, R.P.V.D. and M.C.H. thank the National Science Foundation for a grant from the Major Research Instrumentation Program (CHE03-20751) that enabled construction of the UHV-STM.

■ REFERENCES

- (1) Anderson, M. S. *Appl. Phys. Lett.* **2000**, *76*, 3130–3132.
- (2) Hayazawa, N.; Inouye, Y.; Sekkat, Z.; Kawata, S. *Opt. Commun.* **2000**, *183*, 333–336.
- (3) Stockle, R. M.; Suh, Y. D.; Deckert, V.; Zenobi, R. *Chem. Phys. Lett.* **2000**, *318*, 131–136.
- (4) Neacsu, C. C.; Dreyer, J.; Behr, N.; Raschke, M. B. *Phys. Rev. B* **2006**, *73*, 13406.
- (5) Domke, K. F.; Zhang, D.; Pettinger, B. *J. Am. Chem. Soc.* **2006**, *128*, 14721–7.
- (6) Zhang, W. H.; Yeo, B. S.; Schmid, T.; Zenobi, R. *J. Phys. Chem. C* **2007**, *111*, 1733–1738.
- (7) Hartschuh, A.; Sanchez, E. J.; Xie, X. S.; Novotny, L. *Phys. Rev. Lett.* **2003**, *90*, 095503.
- (8) Saito, Y.; Hayazawa, N.; Kataura, H.; Murakami, T.; Tsukagoshi, K.; Inouye, Y.; Kawata, S. *Chem. Phys. Lett.* **2005**, *410*, 136–141.
- (9) Chan, K. L.; Kazarian, S. G. *Nanotechnology* **2010**, *21*, 445704.
- (10) Stadler, J.; Schmid, T.; Zenobi, R. *ACS Nano* **2011**, *5*, 8442–8448.
- (11) Ogawa, Y.; Toizumi, T.; Minami, F.; Baranov, A. V. *Phys. Rev. B* **2011**, *83*, 081302.
- (12) Budich, C.; Neugebauer, U.; Popp, J.; Deckert, V. *J. Microsc. (Oxford)* **2008**, *229*, 533–539.
- (13) Cialla, D.; Deckert-Gaudig, T.; Budich, C.; Laue, M.; Moller, R.; Naumann, D.; Deckert, V.; Popp, J. *J. Raman Spectrosc.* **2009**, *40*, 240–243.
- (14) Zhang, D.; Domke, K. F.; Pettinger, B. *ChemPhysChem* **2010**, *11*, 1662–1665.
- (15) Binnig, G.; Rohrer, H.; Gerber, C.; Weibel, E. *Phys. Rev. Lett.* **1983**, *50*, 120–123.
- (16) Stipe, B. C.; Rezaei, M. A.; Ho, W. *Science* **1998**, *280*, 1732–1735.
- (17) Smit, R. H.; Noat, Y.; Untiedt, C.; Lang, N. D.; Van Hemert, M. C.; Van Ruitenbeek, J. M. *Nature* **2002**, *419*, 906–9.
- (18) Katano, S.; Kim, Y.; Hori, M.; Trenary, M.; Kawai, M. *Science* **2007**, *316*, 1883–6.
- (19) Ho, W. *J. Chem. Phys.* **2002**, *117*, 11033–11061.
- (20) Steidtner, J.; Pettinger, B. *Rev. Sci. Instrum.* **2007**, *78*, 103104.
- (21) Steidtner, J.; Pettinger, B. *Phys. Rev. Lett.* **2008**, *100*, 236101.
- (22) Forrest, S. R. *Chem. Rev.* **1997**, *97*, 1793–1896.
- (23) Crone, B.; Dodabalapur, A.; Lin, Y. Y.; Filas, R. W.; Bao, Z.; LaDuca, A.; Sarpeshkar, R.; Katz, H. E.; Li, W. *Nature* **2000**, *403*, 521–3.
- (24) Lin, C. F.; Zhang, M.; Liu, S. W.; Chiu, T. L.; Lee, J. H. *Int. J. Mol. Sci.* **2011**, *12*, 476–505.
- (25) Manandhar, K.; Ellis, T.; Park, K. T.; Cai, T.; Song, Z.; Hrbek, J. *Surf. Sci.* **2007**, *601*, 3623–3631.
- (26) Huang, H.; Huang, Y. L.; Pflaum, J.; Wee, A. T. S.; Chen, W. *Appl. Phys. Lett.* **2009**, *95*, 263309.
- (27) Kroger, I.; Stadtmuller, B.; Stadler, C.; Zirotto, J.; Kochler, M.; Stahl, A.; Pollinger, F.; Lee, T. L.; Zegenhagen, J.; Reinert, F.; Kumpf, C. *New J. Phys.* **2010**, *12*, 083038.
- (28) Stadtmuller, B.; Kroger, I.; Reinert, F.; Kumpf, C. *Phys. Rev. B* **2011**, *83*, 085416.
- (29) Kroger, I.; Stadtmuller, B.; Kleimann, C.; Rajput, P.; Kumpf, C. *Phys. Rev. B* **2011**, *83*, 195414.
- (30) Foley, E. T.; Yoder, N. L.; Guisinger, N. P.; Hersam, M. C. *Rev. Sci. Instrum.* **2004**, *75*, 5280–5287.
- (31) Van Duyne, R. P.; Hulteen, J. C.; Treichel, D. A. *J. Chem. Phys.* **1993**, *99*, 2101–2115.
- (32) Baerends, E. J.; Ziegler, T.; Autschbach, J.; Bashford, D.; Bérces, A.; Bickelhaupt, F. M.; Bo, C.; Boerrigter, P. M.; Cavallo, L.; Chong, D. P.; Deng, L.; Dickson, R. M.; Ellis, D. E.; van Faassen, M.; Fan, L.; Fischer, T. H.; Fonseca Guerra, C.; Ghysels, A.; Giammona, A.; van Gisbergen, S. J. A.; Götz, A. W.; Groeneveld, J. A.; Gritsenko, O. V.; Grüning, M.; Gusarov, S.; Harris, F. E.; van den Hoek, P.; Jacob, C. R.; Jacobsen, H.; Jensen, L.; Kaminski, J. W.; van Kessel, G.; Kootstra, F.; Kovalenko, A.; Krykunov, M. V.; van Lenthe, E.; McCormack, D. A.; Michalak, A.; Mitoraj, M.; Neugebauer, J.; Nicu, V. P.; Noodleman, L.; Osinga, V. P.; Patchkovskii, S.; Philipsen, P. H. T.; Post, D.; Pye, C. C.; Ravenek, W.; Rodríguez, J. I.; Ros, P.; Schipper, P. R. T.; Schreckenbach, G.; Seldenthuis, J. S.; Seth, M.; Snijders, J. G.; Solà, M.; Swart, M.; Swerhone, D.; te Velde, G.; Vernooijs, P.; Versluis, L.; Visscher, L.; Visser, O.; Wang, F.; Wesolowski, T. A.; van Wezenbeek, E. M.; Wiesenekker, G.; Wolff, S. K.; Woo, T. K.; Yakovlev, A. L. *ADF*; <http://www.scm.com>, 2010.
- (33) Zhao, L. L.; Jensen, L.; Schatz, G. C. *J. Am. Chem. Soc.* **2006**, *128*, 2911–2919.
- (34) Neugebauer, J.; Reiher, M.; Hess, B. A. *J. Chem. Phys.* **2002**, *117*, 8623–8633.
- (35) Cheng, Z. H.; Gao, L.; Deng, Z. T.; Jiang, N.; Liu, Q.; Shi, D. X.; Du, S. X.; Guo, H. M.; Gao, H. J. *J. Phys. Chem. C* **2007**, *111*, 9240–9244.
- (36) Jiang, N.; Zhang, Y. Y.; Liu, Q.; Cheng, Z. H.; Deng, Z. T.; Du, S. X.; Gao, H. J.; Beck, M. J.; Pantelides, S. T. *Nano Lett.* **2010**, *10*, 1184–8.
- (37) Pettinger, B.; Ren, B.; Picardi, G.; Schuster, R.; Ertl, G. *J. Raman Spectrosc.* **2005**, *36*, 541–550.
- (38) Wustholz, K. L.; Henry, A. I.; McMahan, J. M.; Freeman, R. G.; Valley, N.; Piotti, M. E.; Natan, M. J.; Schatz, G. C.; Van Duyne, R. P. *J. Am. Chem. Soc.* **2010**, *132*, 10903–10910.
- (39) Kleinman, S. L.; Ringe, E.; Valley, N.; Wustholz, K. L.; Phillips, E.; Scheidt, K. A.; Schatz, G. C.; Van Duyne, R. P. *J. Am. Chem. Soc.* **2011**, *133*, 4115–4122.
- (40) Basova, T. V.; Kiselev, V. G.; Schuster, B. E.; Peisert, H.; Chasse, T. *J. Raman Spectrosc.* **2009**, *40*, 2080–2087.
- (41) Murray, C.; Dozova, N.; McCaffrey, J. G.; FitzGerald, S.; Shafizadeh, N.; Crépin, C. *Phys. Chem. Chem. Phys.* **2010**, *12*, 10406–10422.
- (42) Brown, C. J. *J. Chem. Soc. A* **1968**, 2488–2493.